Secondary Electron Interference from Trigonal Warping in Clean Carbon Nanotubes

A. Dirnaichner,[1,2] M. del Valle,[2] K. J. G. Götz,[1] F. J. Schupp,[1] N. Paradiso,[1] M. Grifoni,[2] Ch. Strunk,[1] and A. K. Hüttel[1,*]
[1]Institute for Experimental and Applied Physics, University of Regensburg, 93040 Regensburg, Germany
[2]Institute for Theoretical Physics, University of Regensburg, 93040 Regensburg, Germany
(Received 15 February 2016; revised manuscript received 6 June 2016; published 11 October 2016)

We investigate Fabry-Perot interference in an ultraclean carbon nanotube resonator. The conductance shows a clear superstructure superimposed onto conventional Fabry-Perot oscillations. A sliding average over the fast oscillations reveals a characteristic slow modulation of the conductance as a function of the gate voltage. We identify the origin of this secondary interference in intervalley and intravalley backscattering processes which involve wave vectors of different magnitude, reflecting the trigonal warping of the Dirac cones. As a consequence, the analysis of the secondary interference pattern allows us to estimate the chiral angle of the carbon nanotube.

DOI: 10.1103/PhysRevLett.117.166804

Clean carbon nanotubes (CNTs) are an excellent material system to observe Fabry-Perot interference when highly transparent contacts suppress charging effects [1]. This is often the case in the hole regime of transport in CNTs [2,3]. So far, experiments mostly concentrated on the effects of the linear, Dirac-like part of the CNT dispersion relation, resulting in simple Fabry-Perot (FP) interference [1,4–6]. Its hallmark is an oscillatory behavior of the differential conductance $G(V_g, V_b)$ as a function of both gate voltage V_g and bias voltage V_b, with frequency proportional to the CNT length [1]. On top of this regular oscillation, *slower* modulations are sometimes observed in experiments [1,5,7]. Such secondary interference has been attributed to disorder [7,8] or to channel mixing at the CNT-contact interface [9]. It has been suggested that a slow modulation can also originate from intrinsic interference effects in chiral CNTs [10]. In general, being related to a difference of accumulated phases, secondary interference probes the nonlinearity of the CNT dispersion relation due to the trigonal warping and, in turn, the chiral angle [9,10].

In this Letter, we report on the investigation of a peculiar secondary interference pattern in the hole regime of an ultraclean CNT. Upon averaging over the fast primary FP oscillations, the resulting average linear conductance $\bar{G}(V_g)$ shows a quasiperiodic slow modulation deep in the hole regime. We combine detailed tight-binding calculations and fundamental symmetry arguments to identify the origin of the slow modulation. Our analysis of the gate voltage dependence of $\bar{G}(V_g)$ allows us to estimate the CNT's chiral angle θ.

We measure the differential conductance of a suspended CNT attached to 50-nm-thick Pt/Ti leads, separated by a 1.2-μm-wide trench, at $T = 15$ mK [11]. The fabrication process is optimized to produce defect-free devices [12]. Figure 1(a) displays the conductance $G(V_g, V_b)$ of the CNT device as function of gate voltage V_g and bias voltage V_b. On the electron conduction side ($V_g > 0.35$V, see the Supplemental Material [11]), transport characteristics are dominated by Coulomb blockade. On the hole side, owing to the high transparency of the barriers, the CNT behaves as an electronic 1D waveguide. An oscillatory large conductance $0.2 \lesssim G/G_0 \lesssim 1.8$ ($G_0 = e^2/h$) is observed for gate voltage values $-15\ \mathrm{V} \lesssim V_g \lesssim 0\ \mathrm{V}$. The electron wave vector is affected by both bias and gate voltage, leading to typical rhombic interference structures in the $G(V_g, V_b)$ diagram [1]. A striking feature of our data is the slow modulation of the conductance pattern as a function of V_g, visible as a series of darker and brighter intervals in Fig. 1(a) alternating on a scale of approximately 2 V.

In Fig. 1(b), we show the differential conductance trace $G(V_g)$ for $V_b = 0$. Primarily, we observe a fast oscillation of the conductance at a frequency $f_1 = 12.8\ \mathrm{V}^{-1}$. This fundamental frequency is directly related to the length of the cavity via $f_1 \simeq \alpha e L/\pi\hbar v_F$ [1]. For $v_F = 8 \times 10^5$ m/s [24], we obtain $L \simeq 1$ μm, which is close to the width of the trench. From the period of the fast oscillation $\Delta V_g^{\mathrm{fast}} = 1/f_1$ and the height V_c of the rhombic pattern in Fig. 1(a), we extract the gate voltage lever arm $\alpha = V_c/\Delta V_g^{\mathrm{fast}} = 0.0210 \pm 0.0007$ [1]. On top of the fast oscillations, the slow modulation is visible. Figure 1(c) shows the sliding average $\bar{G}(V_g)$ of the conductance as function of V_g. The peaks of the average conductance are labeled as $n = 1, \ldots, 6$ starting from the band gap. The spacing of the peak positions $E_n = \alpha \Delta V_{g,n}$ decreases for more negative gate voltages V_g.

We perform a discrete Fourier transform (FT) over a Gaussian window [shaded gray in Fig. 1(b)]. The result is plotted in log scale in Fig. 1(d) as a function of frequency and window position. The FT shows regions in V_g with a dominant fundamental frequency component f_1 alternating with regions where the second harmonic with $f_2 = 2f_1$ prevails. These reflect the frequency doubling that is visible in certain ranges of V_g in Fig. 1(b). In these regions, the FT also reveals components from higher harmonic frequencies

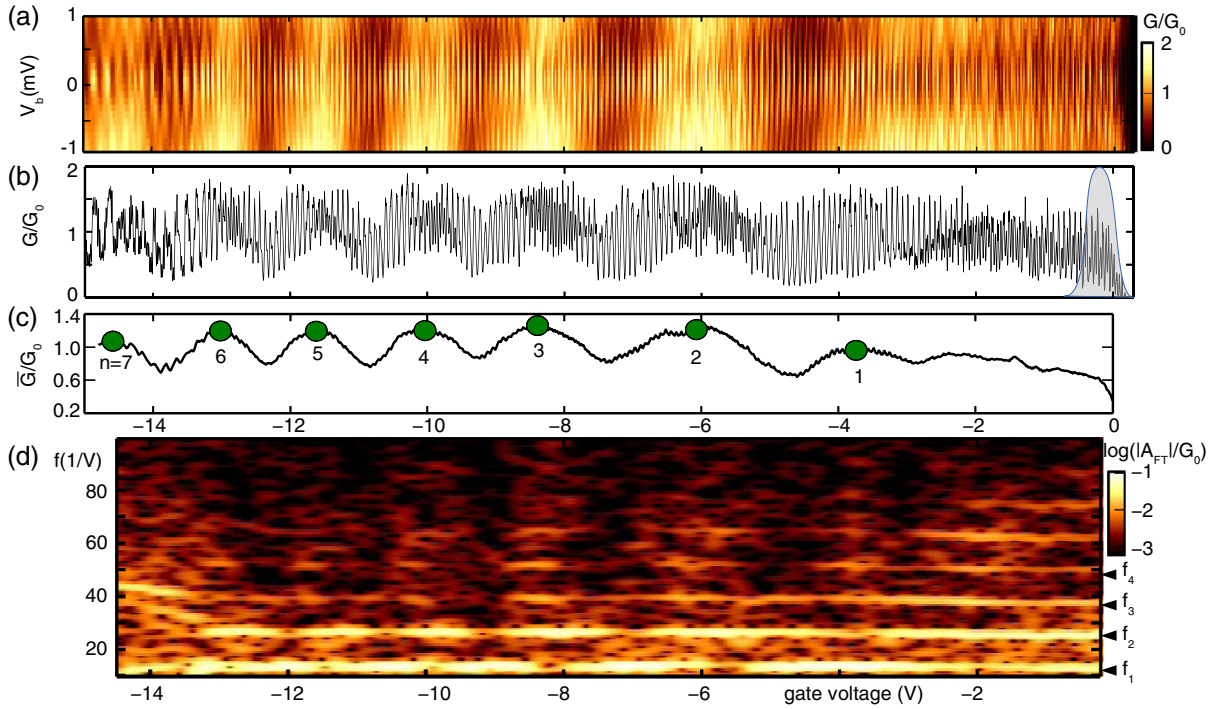

FIG. 1. (a) Differential conductance $G(V_g, V_b)$ of a clean CNT device in the hole conduction regime, as a function of back gate voltage V_g and bias voltage V_b ($G_0 = e^2/h$). (b) Zero bias conductance $G(V_g)$ extracted from (a). (c) Average conductance $\bar{G}(V_g)$ obtained over a sliding 0.4-V-wide Gaussian window. A slow modulation is observed. The peak positions are marked with filled circles. The distance $\Delta V_{g,n} = V_{g,n} - V_{g,n+1}$ between the nth and the $(n-1)$th peak decreases with n. (d) Fourier transform of a sliding 0.4-V-wide window in the signal in (b) as a function of the gate voltage.

$f_n = nf_1$, appearing as horizontal lines in the FT plot. An analysis of the decay of the higher harmonic amplitudes in the Fourier transform yields an average length of the electronic path in the interferometer of 2.7 μm. This length corresponds to the dwell time of an electron in the device and provides a lower bound on its phase coherence length [11]. As shown in Fig. 1(d), the entire spectrum consists mainly of one fundamental frequency and its harmonics; i.e., no additional fundamental frequency occurs. Hence, we can conclude that there are no impurities that subdivide the CNT into a serial connection of multiple FP interferometers [8].

The main features observed in the experiment can be reproduced by a real-space tight-binding calculation, a description that allows us to realistically include curvature effects and the spin-orbit interaction in the real-space Hamiltonian of our system [13,25]. The transport properties of the CNTs are obtained within the Landauer-Büttiker approach, using Green's function techniques, very well suited for transport calculations in the ballistic regime. This numerical approach can be applied to CNTs with arbitrary structure. In Figs. 2(a)–2(d), our numerical results for the transmission of four different classes of CNTs are shown. Strikingly, the slow modulation pattern in the average transmission $\bar{T}$ is observed only for the CNT geometry in Fig. 2(d), where even in an idealized system the absence of certain symmetries (discussed below) allows interferometer channel mixing. As we are going to explain, the crucial geometrical property determining this secondary FP pattern is the chiral angle.

Carbon nanotubes can be grouped in four distinct classes [26–28]: armchair, armchairlike, zigzag, and zigzaglike. The CNT chiral indices (n, m) determine the class: If the ratio of $n-m$ to their greatest common divisor $d = \gcd(n,m)$ is a multiple of 3, i.e., $(n-m)/3d \in \mathbb{Z}$, the CNT belongs to the chiral armchairlike class if $n \neq m$ and is an achiral armchair CNT if $n = m$. Otherwise, we are dealing with a zigzaglike CNT unless $m = 0$, which characterizes achiral zigzag CNTs.

This classification reflects intrinsic differences in the CNT band structure, which are of crucial importance to the transport properties of these systems. In metallic zigzag and zigzaglike CNTs, the π bands cross at the Dirac points $\vec{K} = (k_\parallel = 0, k_\perp = +K_\perp)$, $\vec{K}' = -\vec{K}$ [26]. Here, $k_\parallel$ and $k_\perp$ are the components of the wave vector parallel and perpendicular to the CNT axis. In particular, $k_\perp$ is proportional to the crystal angular momentum that stems from the rotational C_d symmetry and is opposite in the two valleys. When considering reflections from the interfaces, this symmetry only allows for intravalley backscattering. Thus, each valley constitutes an independent transport channel, as depicted in Figs. 2(a) and 2(b). In this case, the FP oscillations are mainly described by the standard expression for the transmission [14]

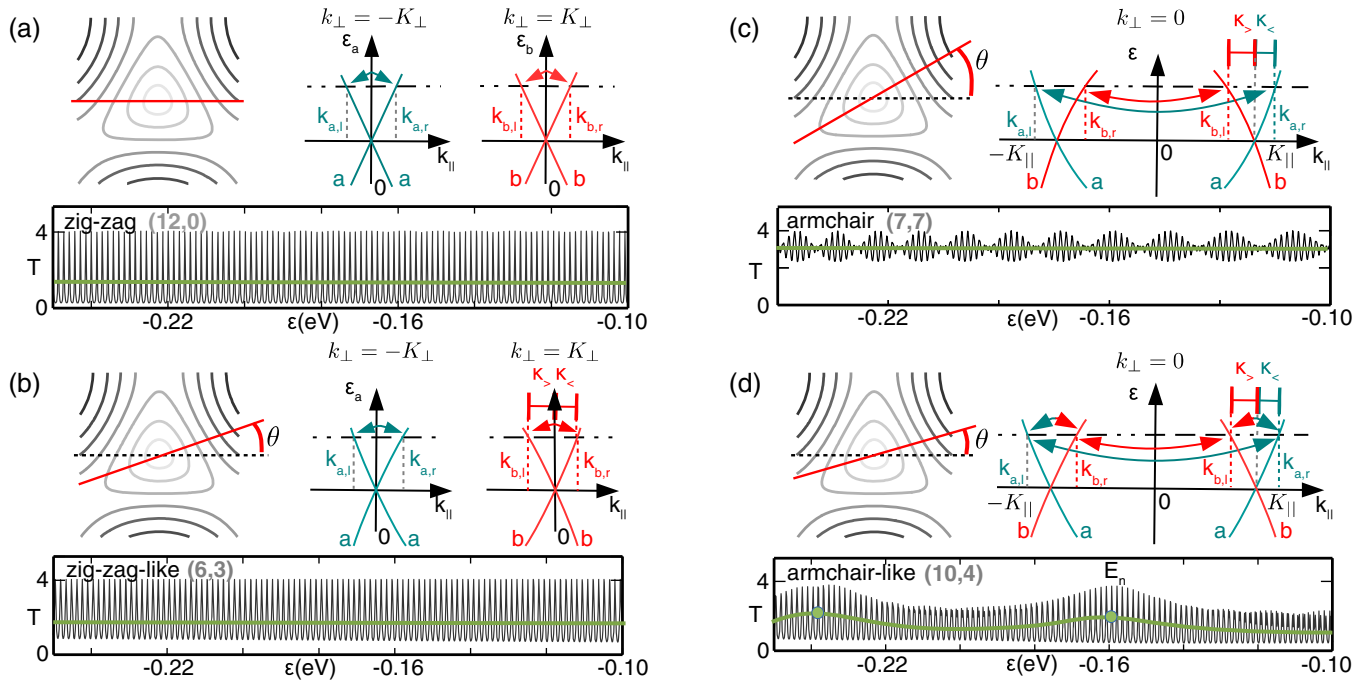

FIG. 2. Graphene dispersion relation $\varepsilon(\mathbf{k})$ (contour plots in the top left panel of each subfigure) in the vicinity of a Dirac point and simplified lowest 1D subbands (line plots, top right) [25]. The solid red line in the contour plot marks the direction of $k_\parallel$. The chiral angle θ is measured with respect to the direction of the zigzag CNT (dashed line). The bottom panels show exemplary transmission patterns obtained by numerical tight-binding calculations. The green line represents the sliding average $\bar{T}$ of the transmission signal. (a) Zigzag: Dispersion relations at the two Dirac points $-K_\perp$ (green) and $K_\perp$ (red) are identical and symmetric with respect to the $k_\parallel = 0$ axis. The transmission curve of a (12,0) CNT shows a simple, single-channel FP interference pattern. (b) Zigzaglike: Right- and left-moving branches within each valley exhibit different wave vectors $k_{j,r/l}$ at finite energy. No intervalley scattering is possible in (a) and (b); see the text. A single-channel-like transmission pattern can be observed for the (6,3) CNT (bottom left). (c) Armchair: Parity symmetry forbids scattering between a and b branches. At finite energy, the two Kramers channels a and b have different wave vectors associated with the right- and left-moving states and a beat in the interference pattern is observed in the tight-binding calculation for the (7,7) CNT. (d) Armchairlike: In the armchairlike CNTs, the parity symmetry is broken and interchannel scattering is enabled (see the text). A slow modulation of the transmission pattern can be observed in the average transmission $\bar{T}$ of a (10,4) CNT (bottom right).

$$\mathcal{T}(V_g) = \sum_{j=a,b} \frac{2|t_1|^2|t_2|^2}{1+|r_1|^2|r_2|^2 - 2|r_1\|r_2|\cos[\phi_j(V_g)]}, \quad (1)$$

where j labels the two independent channels, and the transmission and reflection amplitudes for the two confining barriers are given by t_1, t_2 and r_1, r_2, respectively. The phase accumulated upon one round trip is given by $\phi_j(V_g) = (|k_{j,l}(V_g)| + |k_{j,r}(V_g)|)L$, and the wave vector of the right (left) moving electron $k_{j,r(l)}$ is linked to V_g via the CNT dispersion relation $\varepsilon(k_{j,r(l)}) = \alpha e V_g$. In zigzag and zigzaglike CNTs, the accumulated phases are identical for the two channels since the dispersion in the two valleys is symmetric, i.e., $k_{a,r} = |k_{b,l}|$ and $k_{b,r} = |k_{a,l}|$. According to Eq. (1), one single FP oscillation occurs when $\phi_j = 2\pi$. Consequently, the tight-binding model calculations of a (12,0) CNT in Fig. 2(a) and of a (6,3) CNT in Fig. 2(b) show featureless single-channel interference patterns with a fundamental frequency f_1.

On the other hand, in armchair and armchairlike CNTs, the bands cross at the Dirac points $\vec{K} = (K_\parallel, 0)$ and $\vec{K}' = -\vec{K}$; see Figs. 2(c) and 2(d). Two valleys are formed, which are symmetric with respect to the $k_\parallel = 0$ axis and both characterized by zero crystal angular momentum [26]. Intervalley backscattering is now possible, and the angular momentum quantum numbers do not provide a means to distinguish the transport channels.

However, armchair CNTs are invariant under the parity operation [26], which enables us to identify now two other independent transport channels a and b. These parity channels are such that within one pair, backscattering connects a left mover or right mover in the K valley to its time-reversal partner in the K' valley; see Fig. 2(c). Equation (1) still describes the FP oscillations but, in contrast to the zigzaglike class, the two channels accumulate different phases $\phi_a = 2k_{a,r}L \neq \phi_b = 2k_{b,l}L$, owing to the trigonal warping. In the interference pattern, we thus expect a beat with a constant average transmission. This expectation is confirmed by our tight-binding transport calculations for a (7,7) CNT; see Fig. 2(c).

In armchairlike CNTs, the parity symmetry is absent, and hence backscattering from branch a to branch b in the same valley is also possible. The interference pattern displays

secondary interference with slow oscillations of the average transmission. The occurrence of the slow modulation can be understood from the mode mixing within a simplified model; see the Supplemental Material [11]. This observation is confirmed by the tight-binding modeling of a (10,4) CNT in Fig. 2(d). Our calculation clearly demonstrates that valley mixing effects can occur also in clean CNTs [29] and cannot be taken as an indicator of disorder.

In a realistic experiment, the coupling between the CNT and the metallic contacts differs between CNT top and bottom parts and depends on the fabrications details. In the Supplemental Material, we have investigated the effects of an extrinsic top versus bottom symmetry breaking at the contacts in zigzaglike CNTs. It induces a breaking of the rotational $\mathcal{C}_d$ symmetry and hence allows for transport channel mixing. Tight-binding calculations confirm that then a slow modulation of $\bar{G}$ analogous to the armchairlike case emerges [11].

For a quantitative analysis, we extract the peak positions $E_n = \alpha V_{g,n}$ of the slow modulation of the average conductance $\bar{G}$ [green dots in Fig. 1(c)] and compare these values to theoretical predictions. A simple model (see the Supplemental Material [11]) shows that the slow modulation is governed by the phase difference between Kramers channels $\Delta\phi^\theta(E) = 2(\kappa^\theta_> - \kappa^\theta_<)L$. Here, the $\kappa^\theta_> \geq \kappa^\theta_< \geq 0$ are the longitudinal wave vectors measured from the same Dirac point. In an armchairlike CNT with chiral angle θ, $k^\theta_{a,l} = -K_\parallel - \kappa^\theta_<$, $k^\theta_{b,r} = -K_\parallel + \kappa^\theta_>$, $k^\theta_{b,l} = K_\parallel - \kappa^\theta_>$, and $k^\theta_{a,r} = K_\parallel + \kappa^\theta_<$; see Fig. 2(d). For a zigzaglike CNT, the $\kappa^\theta_{>/<}$ are in analogy given by $\kappa^\theta_> = k^\theta_{a,r} = |k^\theta_{b,l}|$ and $\kappa^\theta_< = |k^\theta_{a,l}| = k^\theta_{b,r}$; see Fig. 2(b). In either case, a peak occurs when

$$\Delta\phi^\theta(E) = 2\pi n. \tag{2}$$

This result is validated by tight-binding calculations [11].

The phase difference $\Delta\phi^\theta(E)$ is computed numerically from the tight-binding dispersion relation $\varepsilon^\theta(k^\theta_{j,i})$ [15]. It is shown for different chiral angles θ in Fig. 3. The slope of $\Delta\phi^\theta(E)$ is monotonically increasing with θ and is 0 for the zigzag case (Fig. 3, left inset) and maximal for the armchair case (right inset). In the model calculation, the energy is measured from the Dirac point. In the experiment, however, the center of the gap is located at $V_g = 0.31$ V. Hence, to check whether the experimental peak positions are determined by Eq. (2), one has to account for an energy shift $\Delta E_{\text{gap}} = \int_{0\text{V}}^{0.31\text{V}} \alpha_{\text{gap}}(V_g) dV_g$, where $\alpha_{\text{gap}}(V_g)$ is the lever arm in the gap region. $\alpha_{\text{gap}}(V_g)$ increases in the vicinity of the band gap starting at $V_g = 0.15$ V until it reaches 0.68 ± 0.03 within the band gap [30]. The dots in Fig. 3 are thus given by the coordinates $(E_n + \Delta E_{\text{gap}}, 2\pi n)$ and are compared to $\Delta\phi^\theta(E)$. The chiral angle θ can thus be used as a fit parameter. The error bars indicate the experimental uncertainty for ΔE_{gap}, which we are only able to restrict to a range 55 meV $< \Delta E_{\text{gap}} <$ 60 meV, and α [11]. The fit

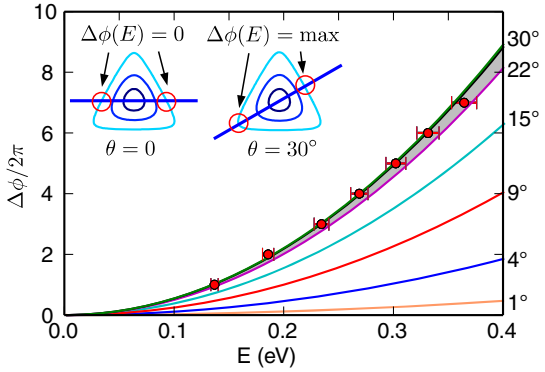

FIG. 3. Computed phase differences $\Delta\phi^\theta$ between modes as a function of energy measured from the Dirac point for different chiral angles θ. The phase difference is a monotonically increasing function of θ starting from the zigzag CNT with $\theta = 0$ (left inset) to the armchair CNT with $\theta = 30°$ (right inset). The filled circles are obtained using the experimental positions $E_n + \Delta E_{\text{gap}}$ of the slow modulation and requiring $\Delta\phi/2\pi = n$. The error bars indicate the uncertainty in α and in ΔE_{gap} (see the text). Acceptable fits are obtained by chiral angles in the range $22° \leq \theta < 30°$ [11], as indicated by the gray shaded area.

provides an estimation of $22° \leq \theta < 30°$ for the chiral angle; see Fig. 3 (gray shaded area).

At high energies, the chiral angle θ and the trigonal warping of the graphene dispersion relation alone determine slope and curvature of the 1D subbands, and thereby the accumulated phase difference between the Kramers channels [11]. In a realistic experiment, there is likely an extrinsic symmetry breaking at the contacts. Thus, channel mixing is expected for both zigzaglike and armchairlike CNTs and in either case allows for evaluation of the chiral angle when several periods of the slow modulation are recorded.

In conclusion, the secondary Fabry-Perot interference provides a robust tool to estimate the chiral angle, a key characteristic that is crucial for understanding carbon nanotube properties such as the spin-orbit coupling [31,32] or the KK' mixing [27]. In contrast to other methods like, e.g., Raman spectroscopy or scanning probe microscopy, which are difficult to combine with transport spectroscopy, our analysis can be easily integrated with measurements in the few-electron or in the Kondo regime.

The authors acknowledge financial support by the Deutsche Forschungsgemeinschaft (Emmy Noether Grant Hu 1808/1, GRK 1570, SFB 689).

*andreas.huettel@ur.de

[1] W. Liang, M. Bockrath, D. Bozovic, J. H. Hafner, M. Tinkham, and H. Park, Fabry-Perot interference in a nanotube electron waveguide, Nature (London) **411**, 665 (2001).

[2] K. Grove-Rasmussen, H. I. Jorgensen, and P. E. Lindelof, Fabry-Perot interference, Kondo effect and Coulomb

blockade in carbon nanotubes, Physica E (Amsterdam) **40**, 92 (2007).
[3] T. Kamimura, Y. Ohno, and K. Matsumoto, Transition between particle nature and wave nature in single-walled carbon nanotube device, Jpn. J. Appl. Phys. **48**, 015005 (2009).
[4] N. Y. Kim, P. Recher, W. D. Oliver, Y. Yamamoto, J. Kong, and H. Dai, Tomonaga-Luttinger Liquid Features in Ballistic Single-Walled Carbon Nanotubes: Conductance and Shot Noise, Phys. Rev. Lett. **99**, 036802 (2007).
[5] H. T. Man, I. J. W. Wever, and A. F. Morpurgo, Spin-dependent quantum interference in single-wall carbon nanotubes with ferromagnetic contacts, Phys. Rev. B **73**, 241401 (2006).
[6] L. G. Herrmann, T. Delattre, P. Morfin, J.-M. Berroir, B. Plaçais, D. C. Glattli, and T. Kontos, Shot Noise in Fabry-Perot Interferometers Based on Carbon Nanotubes, Phys. Rev. Lett. **99**, 156804 (2007).
[7] J. Kong, E. Yenilmez, T. W. Tombler, W. Kim, H. Dai, R. B. Laughlin, L. Liu, C. S. Jayanthi, and S. Y. Wu, Quantum Interference and Ballistic Transmission in Nanotube Electron Waveguides, Phys. Rev. Lett. **87**, 106801 (2001).
[8] F. Romeo, R. Citro, and A. Di Bartolomeo, Effect of impurities on Fabry-Pérot physics of ballistic carbon nanotubes, Phys. Rev. B **84**, 153408 (2011).
[9] J. Jiang, J. Dong, and D. Y. Xing, Quantum Interference in Carbon-Nanotube Electron Resonators, Phys. Rev. Lett. **91**, 056802 (2003).
[10] L. Yang, J. Chen, H. Yang, and J. Dong, Quantum interference in nanotube electron waveguides, Eur. Phys. J. B **43**, 399 (2005).
[11] See Supplemental Material at http://link.aps.org/supplemental/10.1103/PhysRevLett.117.166804, which includes Refs. [1,9,12–23], for additional details on the device fabrication, on the Fourier analysis of the interference pattern, on the transfer matrix and tight binding calculations (including the cases of spin-orbit interaction or broken rotational symmetry), and on the error bounds for the chiral angle.
[12] A. K. Hüttel, G. A. Steele, B. Witkamp, M. Poot, L. P. Kouwenhoven, and H. S. J. van der Zant, Carbon nanotubes as ultrahigh quality factor mechanical resonators, Nano Lett. **9**, 2547 (2009).
[13] M. del Valle, M. Margańska, and M. Grifoni, Signatures of spin-orbit interaction in transport properties of finite carbon nanotubes in a parallel magnetic field, Phys. Rev. B **84**, 165427 (2011).
[14] S. Datta, *Electronic Transport in Mesoscopic Systems* (Cambridge University Press, Cambridge, England, 1997), p. 377.
[15] R. Saito, M. Dresselhaus, and G. Dresselhaus, *Physical Properties Of Carbon Nanotubes* (World Scientific, Singapore, 1998).
[16] D. Hofstetter and R. L. Thornton, Theory of loss measurements of Fabry-Perot resonators by Fourier analysis of the transmission spectra, Opt. Lett. **22**, 1831 (1997).
[17] M. Born, *Principles of Optics: Electromagnetic Theory of Propagation, Interference, and Diffraction of Light* (Pergamon, Oxford, 1964).
[18] D. Tománek and S. G. Louie, First-principles calculation of highly asymmetric structure in scanning-tunneling-microscopy images of graphite, Phys. Rev. B **37**, 8327 (1988).
[19] S. Krompiewski, J. Martinek, and J. Barnaś, Interference effects in electronic transport through metallic single-wall carbon nanotubes, Phys. Rev. B **66**, 073412 (2002).
[20] C. J. Lambert and D. Weaire, Decimation and Anderson localization, Phys. Status Solidi (b) **101**, 591 (1980).
[21] M. Ouyang, J. L. Huang, C. L. Cheung, and C. M. Lieber, Energy gaps in "metallic" single-walled carbon nanotubes, Science **292**, 702 (2001).
[22] J. W. G. Wildöer, L. C. Venema, A. G. Rinzler, R. E. Smalley, and C. Dekker, Electronic structure of atomically resolved carbon nanotubes, Nature (London) **391**, 59 (1998).
[23] J. R. Taylor, *An Introduction to Error Analysis: The Study of Uncertainties in Physical Measurements*, 2nd ed. (University Science Books, Herndon, 1997).
[24] M. S. Dresselhaus, G. Dresselhaus, and P. C. Eklund, *Science of Fullerenes and Carbon Nanotubes: Their Properties and Applications* (Academic, New York, 1996), p. 965.
[25] The inclusion of spin-orbit interaction and curvature effects does not affect our conclusions and is omitted here for clarity. Full calculations are shown in Fig. S4 of the Supplemental Material [11].
[26] A. M. Lunde, K. Flensberg, and A.-P. Jauho, Intershell resistance in multiwall carbon nanotubes: A Coulomb drag study, Phys. Rev. B **71**, 125408 (2005).
[27] M. Marganska, P. Chudzinski, and M. Grifoni, The two classes of low-energy spectra in finite carbon nanotubes, Phys. Rev. B **92**, 075433 (2015).
[28] E. A. Laird, F. Kuemmeth, G. A. Steele, K. Grove-Rasmussen, J. Nygård, K. Flensberg, and L. P. Kouwenhoven, Quantum transport in carbon nanotubes, Rev. Mod. Phys. **87**, 703 (2015).
[29] D. R. Schmid, S. Smirnov, M. Margańska, A. Dirnaichner, P. L. Stiller, M. Grifoni, A. K. Hüttel, and C. Strunk, Broken SU(4) symmetry in a Kondo-correlated carbon nanotube, Phys. Rev. B **91**, 155435 (2015).
[30] The origin of the 60 ± 5 meV band gap in our CNT cannot be explained from the CNT curvature. A curvature induced gap of < 20 meV is estimated for a CNT with $\theta > 22°$. Note that for our analysis, the nature of the small band gap is not crucial. We focus on energies ε larger than 90 meV where the effect of the finite band gap on the dispersion is negligible.
[31] F. Kuemmeth, S. Ilani, D. C. Ralph, and P. L. McEuen, Coupling of spin and orbital motion of electrons in carbon nanotubes, Nature (London) **452**, 448 (2008).
[32] G. A. Steele, F. Pei, E. A. Laird, J. M. Jol, H. B. Meerwaldt, and L. P. Kouwenhoven, Large spin-orbit coupling in carbon nanotubes, Nat. Commun. **4**, 1573 (2013).